Investigating nucleation and growth phenomena in microfluidic supercritical antisolvent process by coupling in situ fluorescence spectroscopy and direct numerical simulation

Thomas Jaouhari, Samuel Marre, Thierry Tassaing, Suzanne Fery-Forgues, Cyril Aymonier, Arnaud Erriguible

Investigating nucleation and growth phenomena in microfluidic supercritical antisolvent process by coupling *in situ* fluorescence spectroscopy and direct numerical simulation

T. Jaouhari[1], S. Marre[1], T. Tassaing[2], S. Fery-Forgues[3], C. Aymonier[1], A. Erriguible[1,4]*

[1]CNRS, Univ. Bordeaux, Bordeaux INP, ICMCB, UMR 5026, F-33600, Pessac Cedex, France
[2]CNRS, Univ. Bordeaux, Bordeaux INP, ISM, F-33405, Talence Cedex, France
[3]SPCMIB, UMR CNRS 5068, Université Toulouse III Paul-Sabatier, 118, route de Narbonne, 31062 Toulouse Cedex 09, France
[4]CNRS, Univ. Bordeaux, Bordeaux INP, I2M, UMR 5295, F-33600, Pessac Cedex, France

ABSTRACT

High-pressure microfluidic systems exhibit favorable capacity to enhance mixing quality compared to conventional macroscale liquid systems. These mixing conditions (temperature, pressure, design, flowrates) are very interesting for the preparation of fluorescent organic nanoparticles by supercritical antisolvent process. In this work, fundamental mechanisms of microfluidic supercritical antisolvent process (μSAS) including thermodynamics, hydrodynamics, nucleation and growth phenomena, are investigated using a coupled experimental/simulation approach. Specifically, we are demonstrating the experimental determination of the particle precipitation field in a CO2 / solvent medium using a fluorescent organic dye molecule, the styrylbenzoxazole derivative (BZX), as a model case for its relevant optical properties. BZX compound presents an enhancement of fluorescence intensity in its aggregated state (AIE effect), which allowed monitoring the *in situ* precipitation in a microreactor. The results of the direct numerical simulation taking into account all the physical phenomena are then compared with the experimental results for validation and deep understanding of the fundamental mechanisms. It is shown that despite ultra-short mixing time, the supersaturation field showed some fluctuation leading to variation of the nucleation times.

INTRODUCTION

In the blooming field of nanomedicine, carrier-free nanodrugs, composed in large part if not entirely of pharmacologically active molecules, have great potentials for the delivery of hydrophobic drugs (Wen et al., 2017; Yang et al., 2019; Zhang et al., 2016; X. Zhang et al., 2020). Compared with traditional

nanocarriers (e.g. liposomes, micelles, polymer, dendrimers, etc.), they possess maximal drug loading capacity, improved pharmacokinetics, reduced toxicity and clear metabolism. The active ingredients which could assemble into carrier-free nanodrugs include drugs and pro-drugs with different mechanisms of therapy, targeting agents, photosensitizers and dye molecules. This approach enables synergistic chemotherapy and the combination of chemotherapy with active targeting, phototherapy and drug delivery control. However, there is urgent demand in developing a simple and "green" method to fabricate carrier-free nanodrugs without toxic solvents, while keeping close control over the nanoparticle (NP) size. For this purpose, several manufacturing processes for organic compounds have been developed (Ding et al., 2016). Among the current conventional precipitation approaches the antisolvent processes are the most commonly employed. The underlying principle of these processes consists in mixing a solute solution with an antisolvent phase to generate supersaturation, which subsequently induces the precipitation of the desired molecules. The micromixing, therefore, has a significant effect on the particle size and size distribution that need to be controlled (Bałdyga et al., 2010). Indeed, a homogeneous concentration distribution and a high degree of supersaturation can only be reached through an intense micromixing. Although the antisolvent can be a gas, a liquid, or a supercritical fluid, a better mixing is achieved with the latter. CO_2 is the predominantly used fluid in supercritical antisolvent processes thanks to its chemical inertness and its mild critical conditions of temperature and pressure (31°C and 7.38 MPa, respectively). Such conditions are well suited for processing fragile organic molecules. Furthermore, it is important to note that the CO_2 technology fits the goal of process sustainability, with a design that enables a one-stage operation, thereby minimizing the energy consumption and the environmental impacts, whilst limiting the purification steps between the operations.

Although supercritical AntiSolvent (SAS) processes are mostly used in semi-continuous mode within macroscopic reactors, nowadays continuous micro- and milli-scale reactors appear to be one of the most promising ways to intensify and better control the process. As these microfluidic systems reduce the time and space scales, their effectiveness in controlling mixing and enhancing the performances of the processes is evident. This is especially true for materials synthesis, for which fast and homogeneous mixing is the key to obtain a narrow size distribution of particles. A recent study (Jaouhari et al., 2020) has shown that a combination of the two types of intensification, supercritical fluids and microfluidic reactors (μSAS), can significantly improve the performance and reproducibility of antisolvent processes. Moreover, it has recently been proven that turbulent conditions can be achieved in high pressure microfluidic devices (F. Zhang et al., 2020), resulting in ultra-fast mixing times as small as 10^{-4}-10^{-5} s, which are highly favorable for the synthesis of organic nanoparticles. In this system, the mechanisms of nucleation and growth are responsible for size and morphology of nanoparticles that directly affects the solubility and bioavailability of organic compounds.

Therefore, the investigation of these mechanisms is essential for a better understanding of the impact of the operating parameters over the final size of synthesized particles. For this, a coupled

experimental/simulation approach is used. High-pressure microfluidic platform offers optical access and well-controlled operating conditions to study *in situ* the precipitation. Our experimental strategy consists in combining microfluidics with an organic fluorogen to visualize *in situ* the precipitation of fluorescent organic nanoparticles (FONs) in the reactor. For that, we take advantage of the specific optical properties of dye molecules that exhibit aggregation induced emission (AIE) effects, *i.e.*, molecules that emit much more strongly in the aggregated and solid states than in solution (Guo et al., 2020; Mei et al., 2015; Wang et al., 2019; Zhao et al., 2020). This type of molecule has already been used to study nucleation and crystallization processes (Ito and Oka, 2019; Tran et al., 2016). To the best of our knowledge, this kind of experiments, leading to on-line visualization of the precipitation by combining microfluidic and AIE fluorogens, has only been performed for low pressure and laminar system (Tran et al., 2016) but not for turbulent flow in supercritical conditions. The fluorescence intensity fields obtained experimentally are then compared to direct numerical simulation, allowing capturing all the mixing scales and considering all the implied phenomena, *i.e.*, thermo-hydrodynamics as well as nucleation and growth. This comparison leads to a better understanding and to the identification of the nucleation mechanisms occurring in the μSAS process. Furthermore, the analysis of the characteristic precipitation time, micromixing time, nucleation time and growth time is discussed to emphasize the role of micromixing in this process.

MATERIALS AND METHODS

Experimental section

Chemicals

Carbon dioxide was purchased from Messer. Tetrahydrofuran (THF), inhibitor-free, ≥ 99.9 %, was purchased from Sigma-Aldrich and used as received. (E)-2-(3-(4-(5-Methoxybenzo[d]oxazol-2-yl)styryl)-5,5-dimethylcyclohex-2-en-1-ylidene)malononitrile (BZX) was synthesized following a previously reported procedure (Bremond et al., 2021).

High Pressure FTIR solubility measurements

As mentioned above, the thermodynamic properties of the {CO_2/solvent/solute} ternary system are important in the SAS process. The measurements were performed in a high-pressure optical cell (HPOC) equipped with silicon windows, which was previously described elsewhere (Jaouhari et al., 2020). In brief, the set-up allows the control of both the pressure and the temperature. Once the equilibrium is reached under stirring conditions, the stirring is stopped and the particles settled down at the bottom of the HPOC. Then, the concentration of each species are measured in a homogeneous fluid phase using a FTIR optical probe to acquire the FTIR spectrum of the mixture {CO_2/solvent/solute}. The absorbance

of the signal can then be directly linked to the concentration of the species, following the Beer Lambert's law. As mentioned in a previous study, there is no shift of the baseline, which could be characteristics from a non-homogeneous medium, thus validating a homogeneous mixture.

Microreactor design and set-up

A Pyrex/silicon microchip was manufactured following standard photolithography / wet etching / anodic bonding protocol (Marre et al., 2010). The microreactor is used as a micromixer to contact the concentrated solution and the antisolvent sc-CO_2, beneficiating from ultra-low mixing times at supercritical conditions . The design of the reactor (Fig. 1a,b) includes a main channel (trapezoidal crossed section, 200 µm deep, 350 µm wide at the top of the channel) in which a silica capillary (ID: 100 µm, OD: 170 µm, from Polymicro©) is inserted and further epoxy-glued to ensure leak-free operations. This results in a 3D coaxial configuration for the contacting point. The microreactor is placed horizontally on a rectangular heating element allowing the control of the temperature. The concentrated solution is injected with a HPLC pump (Jasco PU-4180) inside the capillary, while the CO_2 is injected with a SFC CO2 pump (Jasco PU-4380) into a side channel to ensure its pre-heating before entering the main channel. A filtering cell is placed downstream the microreactor to collect the processed particles. Finally, an automated backpressure regulator (Jasco BP4380) is used at the very end of the continuous process to control the pressure inside the set-up (Fig. 1c).

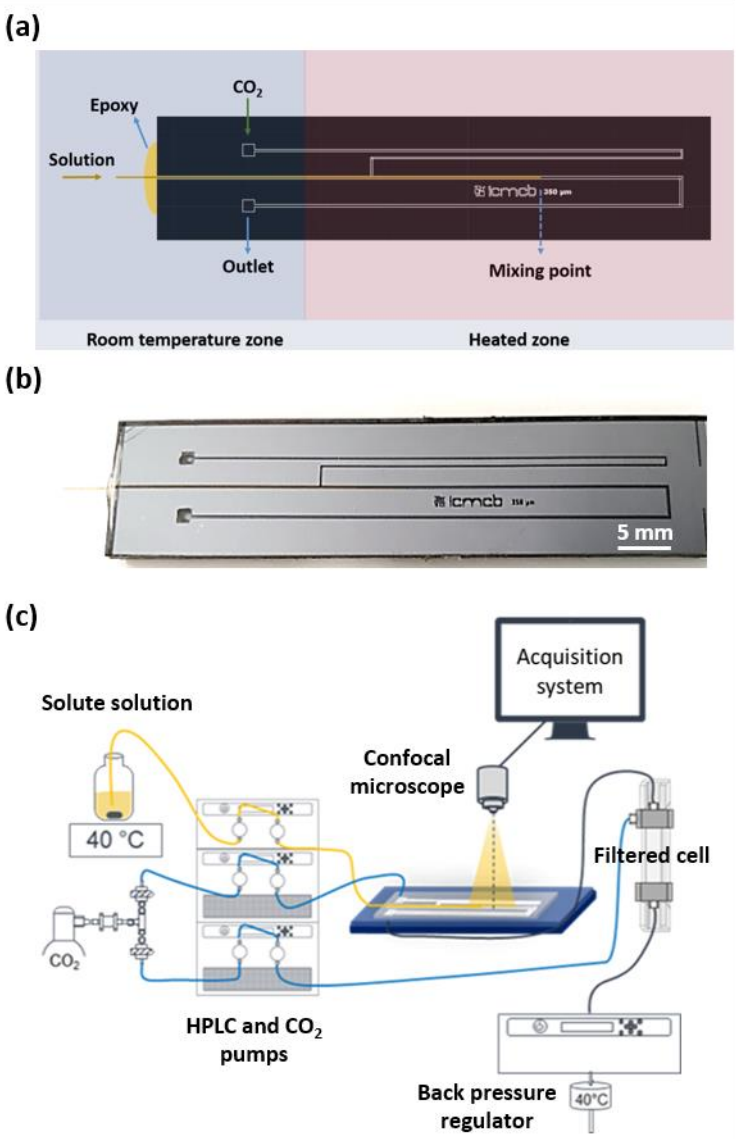

Figure 1: a,b) High pressure microchip; c) Schema of µSAS set-up with confocal microscope for direct visualization.

Choice of the organic compound with aggregation induced emission (AIE) behaviour

The confocal microscope is equipped with a laser diode with an excitation wavelength of 405 nm. The fluorescent molecule BZX (Fig. 2a) was selected because its intense absorption band peaking at 408 nm in THF closely fits this excitation wavelength, and because its enhanced emission in the solid state had been reported in the literature (Yadav et al., 2015). The emission properties of this compound were thoroughly analyzed in a previous work (Bremond et al., 2021). In Figure 2b, we have varied the molar ratio of THF (solvent) and water (antisolvent) from 0 to 100%, leading to an increasing amount of precipitated BZX particles. It appeared that BZX is indeed very weakly emissive in organic solutions when it is dissolved, *e.g.*, the fluorescence quantum yield Φ_F is about 5.1×10^{-3} in THF. Oppositely, the microcrystalline powder emits very strongly ($\Phi_{PL} = 2.8 \times 10^{-1}$, $\lambda_{max} = 606$ nm) at high water content

when the antisolvent leads to massive precipitation. The study of aggregation in THF containing increasing concentration of water shows that the emission intensity markedly increases with the formation of microparticles. This AIE effect is therefore confirmed. Meanwhile, the maximum emission is gradually shifted from 558 nm for solutions in THF to 584 nm at 95% water content (Fig. 2b,c,d). Compound BZX thus appeared as a good candidate for imaging the precipitation zone in the microchannel.

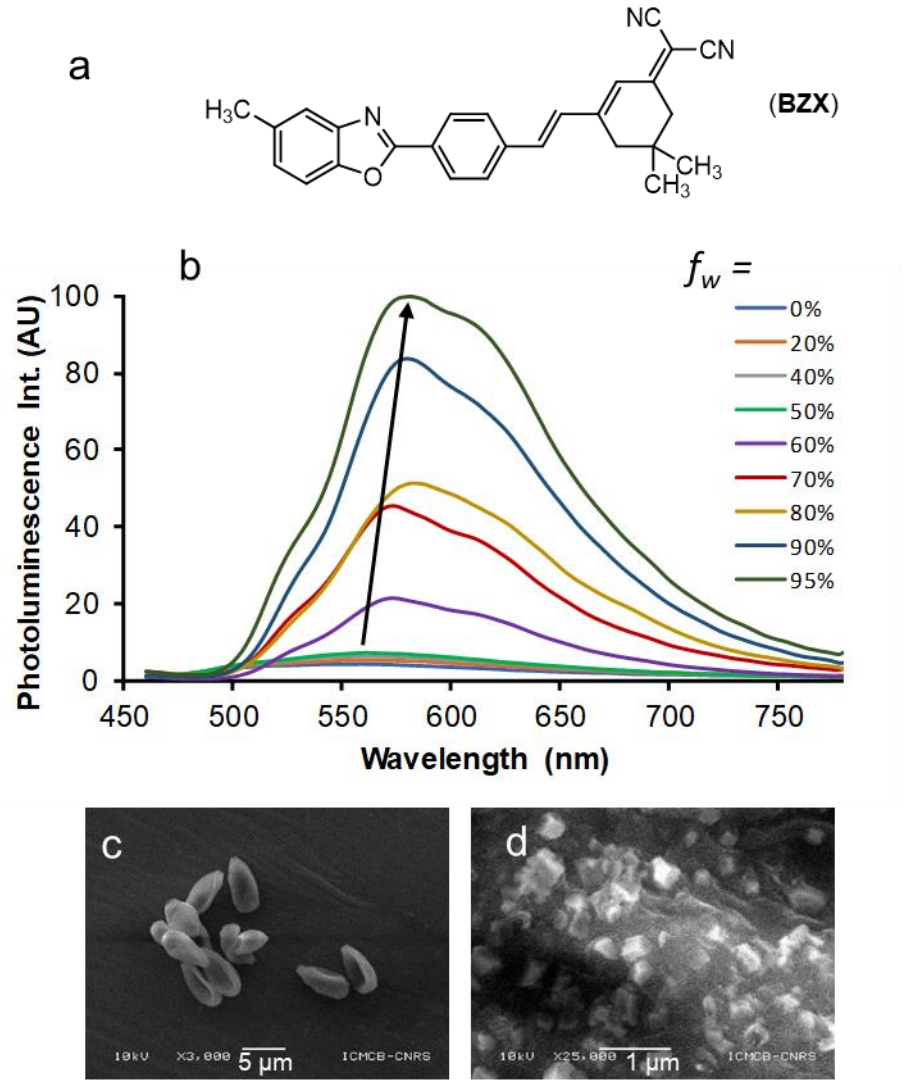

Figure 2: a) Molecular structure of compound BZX. b) Evolution of the photoluminescence spectrum of BZX (7×10^{-6} M) with increasing the water fraction (f_w) in the THF/water mixture. c and d) Scanning electron microscopy images of the particles contained in the suspensions of dye BZX at fw = 60% (amorphous particles) and 95% (microcrystals), respectively.

Confocal microscope and temporal analysis of fluorescence intensities

The microreactor is placed under a confocal microscope for the *in situ* imaging of the FONs fluorescence during the precipitation process. A motorized Leica SP8 confocal microscope is used for direct visualization using an excitation laser diode emitting at 405 nm with an 10× objective (model: HC PL Fluotar 10x/0.30), leading to a resolution of ≈ 1 pixel/µm.

We performed temporal analysis of the fluorescence intensities to quantify a concentration field of fluorescent particles. The temporal analysis was performed in a confocal mode using a point-by-point spectrum analysis. Since we were working under flow conditions, we averaged the measurements out of 100 acquisitions, demonstrating that the mean intensity was attained after less than 100 images. Figure 3 shows typical fluorescence images depending on the number of acquired images, demonstrating the interest of averaging a large number of images to correctly reconstruct the observed area.

We chose the highest acquisition speed (1.92 images.s^{-1}) to observe the microchannel in its entire width, acquiring spectrum between 410 and 750 nm at a spectral resolution of 3 nm. This very important result is compared with the particle field calculated by the simulation and makes it possible to localize the nucleation/precipitation zones in the reactor. This analysis element is essential in the validation of the precipitation models used.

It can be noted that the capillary is coated with a polyimide layer, which exhibits fluorescence under a 405 nm excitation wavelength. However, as this fluorescence was always constant (at the same laser power), it did not affect the measurements intensities from experiment to experiment.

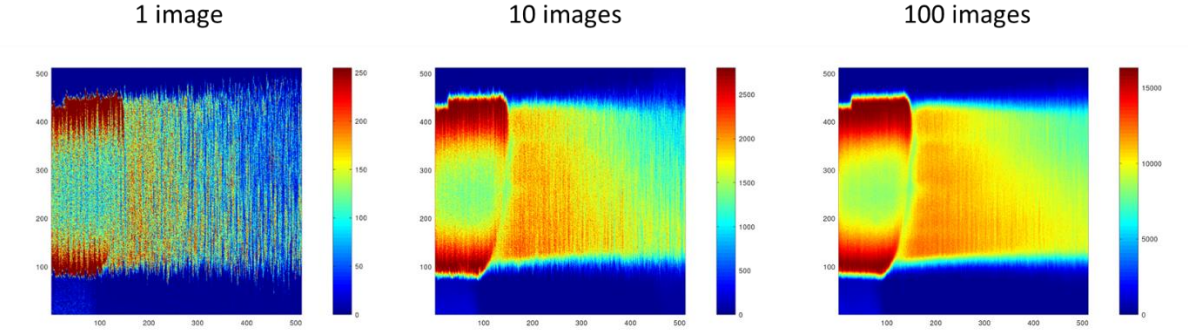

Figure 3: from left to right : microchannel fluorescence imaging obtained from the sum of 1, 10 and 100 images.

Transmission electron microscopy (TEM)

TEM grids were placed inside the filtering cell during the processing of the FONs. Once collected, they were dried, and directly analyzed with a JEOL JEM-1400+ transmission electron microscope for the characterization of organic NPs. A working tension of 60 kV was chosen to avoid any issue with the potential deterioration or melting of the organic NPs during characterization. The obtained TEM images were processed with the ImageJ software for size measurements. Careful attention was brought to the measurement of the particle size, because the determination of surface tension requires to compare simulation results with precise experimental particle size distributions. Therefore, only well-defined particles were considered. Thanks to the large number of recovered particles, it was possible to use several images from the same TEM grid with the same magnification (×50000) to count more than 100 particles per experiment.

Numerical section

The numerical approach allows taking into account all the physical phenomena involved in the process. The method consists in the coupling between a computational fluid dynamics (CFD) code, to consider the thermo-hydrodynamic effects, and a population balance equation (PBE) to take into account the nucleation and growth of particles.

Hydrodynamic and thermodynamic contributions

As the operating conditions are chosen to be far above the mixture critical point, the hydrodynamics equations (continuity and Navier Stokes equations) are solved for an incompressible single phase flow considered as a Newtonian fluid. The simulation is performed down to the Kolmogorov scale so no turbulence model is needed (F. Zhang et al., 2020). It reads:

$$\boldsymbol{\nabla}.\mathbf{u} = 0, \tag{1}$$

$$\rho\left(\frac{\partial \mathbf{u}}{\partial t} + \mathbf{u}.\boldsymbol{\nabla}\mathbf{u}\right) = -\boldsymbol{\nabla}p + \boldsymbol{\nabla}.\left(\mu\left(\boldsymbol{\nabla}\mathbf{u} + \boldsymbol{\nabla}^{\mathrm{T}}\mathbf{u}\right)\right), \tag{2}$$

in which p is the pressure, ρ the density of the fluid, μ the dynamic viscosity, t the time and $\boldsymbol{u}$ the velocity vector. The Peng Robinson equation of state (PR-EOS) with quadratic mixing rules is used for calculating the density of the fluid.

The species continuity equations are expressed by considering advection and ideal diffusion (Zhang et al., 2019) of species according to the Fick's law:

$$\rho\frac{\partial \omega_{THF}}{\partial t} + \boldsymbol{\nabla}\cdot(\rho\omega_{THF}\boldsymbol{u} + \rho D_{THF}\boldsymbol{\nabla}\omega_{THF}) = 0, \tag{3}$$

$$\rho\frac{\partial \omega_s}{\partial t} + \boldsymbol{\nabla}\cdot(\rho\omega_s\boldsymbol{u} + \rho D_s\boldsymbol{\nabla}\omega_s) = -3\rho_p k_v Gm_2, \tag{4}$$

with ω_{THF} and ω_s the mass fractions of solvent and solute, respectively, D_a and D_s the diffusion coefficients of solvent and solute in solvent/CO_2, respectively. ρ_p is the density of the solid solute and k_v the volume shape factor of the particles that is based on the morphology of spherical produced particles ($k_v = \pi/6$).

The mixture viscosity is computed by classical logarithmic mixing rules. The viscosities of the pure fluids, CO_2 and THF, are obtained from the NIST database for the considered experimental conditions.

Nucleation and growth phenomena

As in our case, the precipitated particles obtained experimentally in the microreactor are very small, we assume that the effect of the breakage and the agglomeration can be neglected. According to the conservation law, the general equation of population balance is defined by (Voisin et al., 2017):

$$\rho \frac{\partial n(L,x,t)}{\partial t} + \boldsymbol{\nabla} \cdot \left(\rho \boldsymbol{u} n(L,x,t)\right) + \rho \frac{\partial n(L,X,t)G}{\partial L} = 0. \quad (5)$$

In this equation *n* represents the number density function which depends on internal coordinates (particle size *L*) and external coordinates (space coordinates X (x,y,z)). *G* is the growth rate of the particles. The population balance equation is solved with the standard method of moments. Only the four first moments are solved, the system of equations to be solved remains:

$$\rho \frac{\partial m_j}{\partial t} + \boldsymbol{\nabla} \cdot \left(\rho m_j \boldsymbol{u}\right) = \rho\left(0^j B - jGm_{j-1}\right), \text{ for } j = 0, 1, 2, 3 \quad (6)$$

where m_j is the j[th] moment of the distribution ($m_j = \int_0^\infty n(L,X,t)L^j dL$) and *B* and *G* represent the nucleation and the growth rates.

Considering the experimental distribution, the numerical one is determined by assuming that the distribution is normal. The following relationship is used to build the simulated particle size distribution with the calculated moments:

$$N(L) = \frac{1}{\sigma\sqrt{2\pi}} \exp\left(-\frac{(L-\bar{L})^2}{2\sigma^2}\right), \quad (7)$$

with $\bar{L}$ and σ^2 the mean particle size and the variance of the distribution, respectively.

Nucleation and Growth parameters

The supersaturation is therefore considered as the driving force for precipitation. This dimensionless quantity is defined by:

$$S = \frac{x_s}{x_{sat}}, \quad (8)$$

with x_s and x_{sat} the molar fraction of BZX and the solubility (in mol/mol) respectively.

We have therefore considered in the simulations the only primary nucleation whose frequency is calculated by the following relationship (Mersmann, 1999):

$$B = 1.5 D_{WC} (C_{sat} S N_a)^{7/3} \sqrt{\frac{\sigma}{k_b T}} V_M exp\left(-\frac{16\pi}{3}\left[\frac{\sigma}{k_b T}\right]^3 \frac{{V_M}^2}{ln^2(S)}\right), \quad (9)$$

with N_a the Avogadro constant, σ the solid-fluid interfacial tension, C_{sat} the solubility concentration, k_b the Boltzmann constant and V_m the solute molecular volume, D_{WC} the solute diffusion coefficient (Wilke and Chang, 1955).

The growth rate, assuming that the main mechanism for growth is diffusion, is calculated by:

$$G = \frac{M_p k_a}{3\rho_p k_v} k_g C_{sat}(S-1), \quad (10)$$

where M_p, ρ_p, k_a, k_v and k_g represents respectively the molar mass of the solute, the density of the solute, the surface form factor (equal to π for spherical particles), the volume form factor and the mass transfer coefficient deduced of the local Sherwood number. This one is estimated by the Froessling equation.

Numerical methods

Partial derivatives equations 1-4 and 6 are solved by the homemade Fortran CFD code "Notus" (https://notus-cfd.org/), developed at the Institute of Mechanical Engineering (I2M-TREFLE). Notus is an open source software based on the finite volume method with fixed staggered grid. The CFD code is massively parallel which allows for simulating 3D configuration with great precision. An explicit formulation is used except for the pressure correction step in the velocity-pressure coupling algorithm which is solved implicitly (Jost et al., 2020). The Navier-Stokes equation is solved in two steps by the time-splitting algorithm of Goda (Goda, 1979). The advection term is discretized by the second order scheme in space (total variation diminishing with superbee flux limiter function (TVD superbee)) (Roe, 1986) and an explicit second order central discretization is applied in space for the diffusion term.

Due to the trapezoidal asymmetrical geometry (Figure 4), a three-dimensional simulation is required. As demonstrated in our previous study (F. Zhang et al., 2020), the Kolmogorov and Batchelor scales in our system are in the micrometer range. So we chose an uniform mesh, the grid size of which is $\Delta x = \Delta y = \Delta z = 3\mu m$ for a total number of nodes of 14.5 millions for a channel length of 4 mm. This is a good compromise between precision and CPU time.

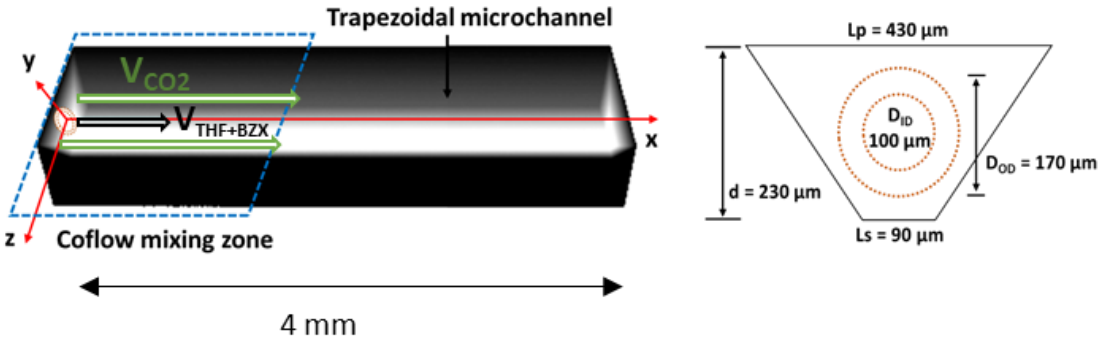

Figure 4: The geometry of the numerical microchannel for the simulations showing the three dimensional trapezoidal microchannel and the dimension of the cross-section at x = 0.

RESULTS AND DISCUSSION

Solubility data of BZX: Solubility data are essential to compute the supersaturation in the simulation. In a first step, we have studied the solubility of the fluorescent compound in the {THF/CO_2} system. The *in situ* infrared spectrometry study allows us to measure the absorbance of each compound under our synthesis conditions: 40 °C and 100 bar. Different experiments are performed by varying the initial volume of THF in the IR HPOC cell. The results of the BZX solubility measurement are presented as a function of the molar fraction of CO_2, related to the initial volume of THF (Figure 5).

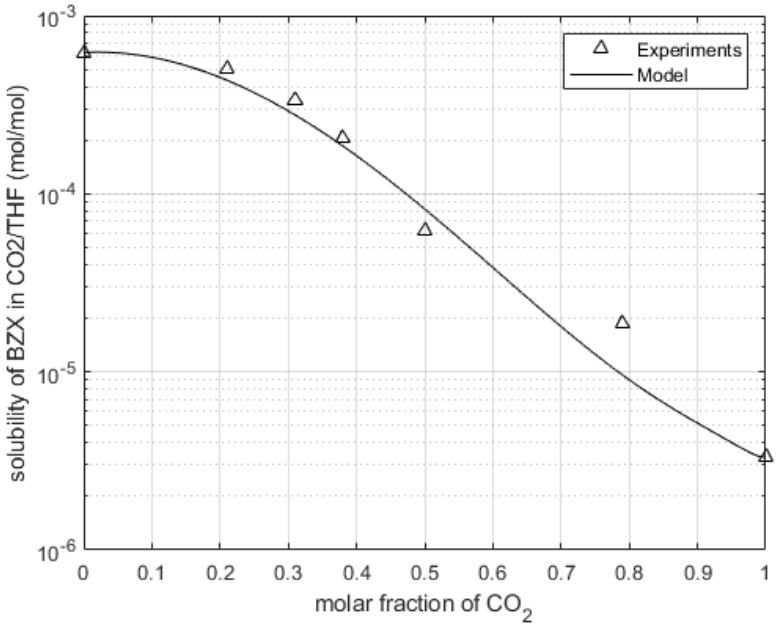

Figure 5: Solubility of BZX in (THF/CO_2) system

Experimental measurements are fitted with the following simple analytical law:

$$x_{sat} = 0.000622(1 - x_{CO2})^{-0.426+11.19x_{CO2}-8.877x_{CO2}^2} + 3.31e^{-6}x_{CO2} \quad (11)$$

with x_{CO2} and x_{sat} the molar fraction of CO_2 and the solubility (in mol/mol) respectively.

Ex-situ analysis of synthetized powder and determination of the solid/fluid surface tension: Experiments were performed according to the operating conditions reported in Table 1. These conditions have been determined in a previous study to offer favorable mixing conditions for materials synthesis.

Our first objective is to analyze *ex situ* the produced powders to determine the experimental particle size distribution. These data are essential to fit our only unknown parameter of the nucleation frequency, the interfacial tension between the solid and the fluid mixture.

The powders recovered at the exit of the microchip were characterized by transmission electron microscopy (Fig. 6).

Table 1: operating conditons of the µSAS experiments

T (°C)	P (bar)	Q_{CO2}(ml/min)	Q_{THF}(ml/min)	[BZX] (mg/ml)
40	100	8	0.44	0.5

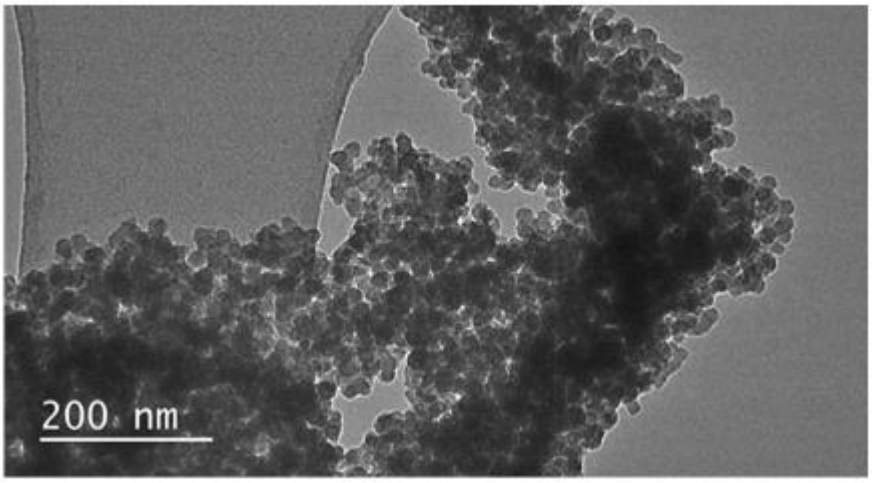

Figure 6: TEM images of nanoparticles of BZX synthesized by µSAS.

The interfacial tension was fitted in order to determine the "numerical" normal particle size distribution close to the experimental one. Comparisons for three values of interfacial tension are shown (Fig. 7). A value of 4.75 mN/m seems to be satisfactory. This value is of the same order of magnitude as that determined for a similar molecule (Jaouhari et al., 2020). It is important to note that while the mean size of the distribution is well estimated, around 16 (± 4) nm, the standard deviation of the "numerical" distribution is much larger, leading to a wider "numerical" distribution. This unexpected result will be discussed after analyzing and comparing the results obtained from the *in situ* experiments and from the simulation.

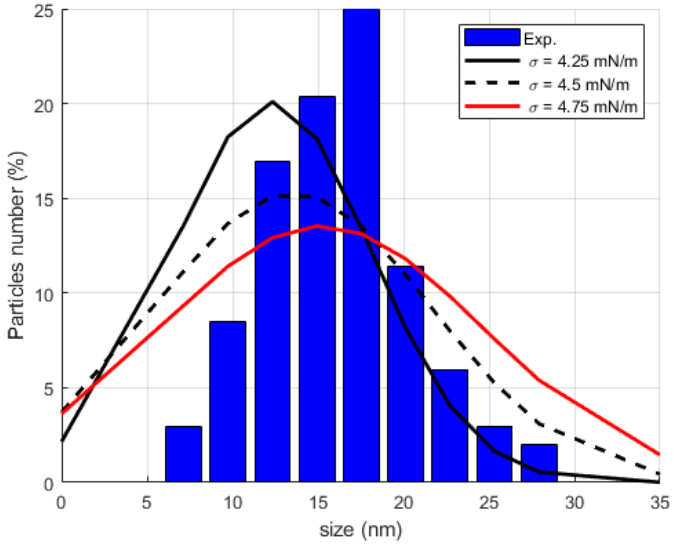

Figure 7: Experimental and simulated size distributions.

In situ analysis of fluorescent intensities and comparison with the simulation

The *in situ* experiment concerned the determination of the fluorescence intensity fields in the microchannel. Fig. 8 (left) displays the intensity mapping obtained experimentally by averaging 100 instantaneous fields. These data allow us to locate the areas where the solid fluorescent particles are present. The intensity field increases with the particle concentration. In figure 8, the abscissa 0 corresponds to the outlet of the injection capillary. The first result obtained shows a very strong intensity signal at the injector outlet. This means that compound BZX precipitates out of the injector. We observe two regions symmetrical to the centre of the capillary where the fluorescence intensity is maximal. It is important to note that the fluorescence intensity drops rapidly as soon as it leaves the injector, at a distance of about 200-300 µm. On the right side of Figure 8, we have represented several maps of the particle concentration in the channel for different heights obtained by numerical simulation. The average "numerical" field is obtained after averaging more than 10,000 instantaneous fields. The comparison of the "numerical" and "experimental" fields shows a great coherence in terms of location of the nucleation/precipitation zones. The simulation shows a strong decrease of the particle intensity/concentration in a zone located between 200 and 300 µm after the exit of the injector. It should be noted that, depending on the height in the capillary, the potential core area in the centre, *i.e.* the area containing only the solution in fluid form, varies significantly, as expected. On the other hand, although some preliminary work has been done to focus the microscope in a plane located at the centre of the capillary, part of the signal of the "defocused" fluorescent particles is certainly recorded by the confocal microscope. This overpopulation of observed particles, especially in the potential core area, explains the difference in appearance between the experimentally reconstructed field and the numerical maps.

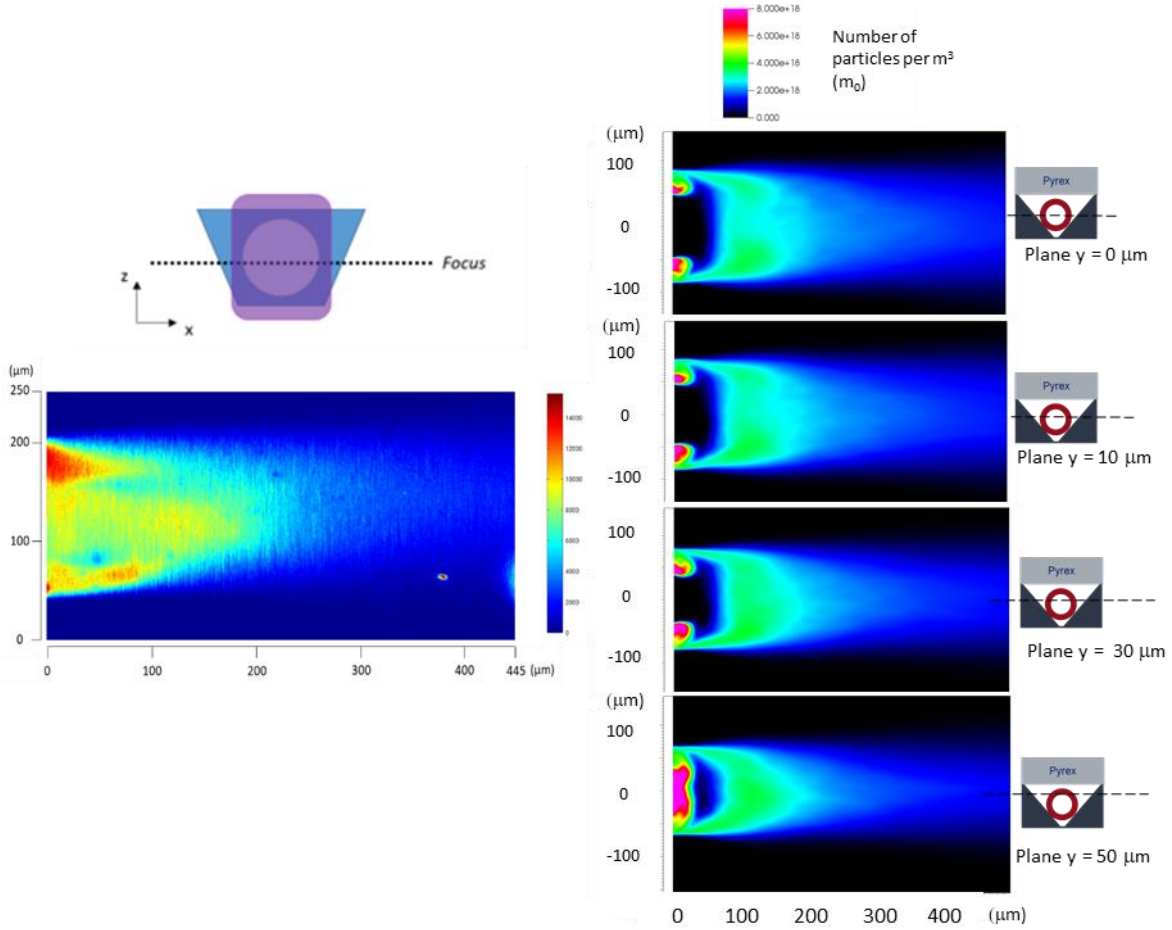

Figure 8: Mapping of time averaged intensity field of particles of BZX in the microchannel (left). Simulation of particle number field in the microchannel having the same dimensions as the experimental one (right).

Figure 9 shows the fluorescence intensity of the particles at different sections of the microchannel. The first section corresponds to the outlet zone of the injector, which is very rich in particles. The second zone, from 500 µm to 1 mm, corresponds to a zone where the intensity is much lower. This tells us that precipitation only takes place in a very short area after the injector. The particles are then dispersed in the channel. The experimental observation is supported by the numerical mapping (Fig. 9). The experimental/numerical comparison is very good and allows us to consider that the nucleation and growth mechanisms chosen for the numerical simulation seem relevant. Indeed, the nucleation seems to take place only in the reactor volume, typical of the primary homogeneous nucleation.

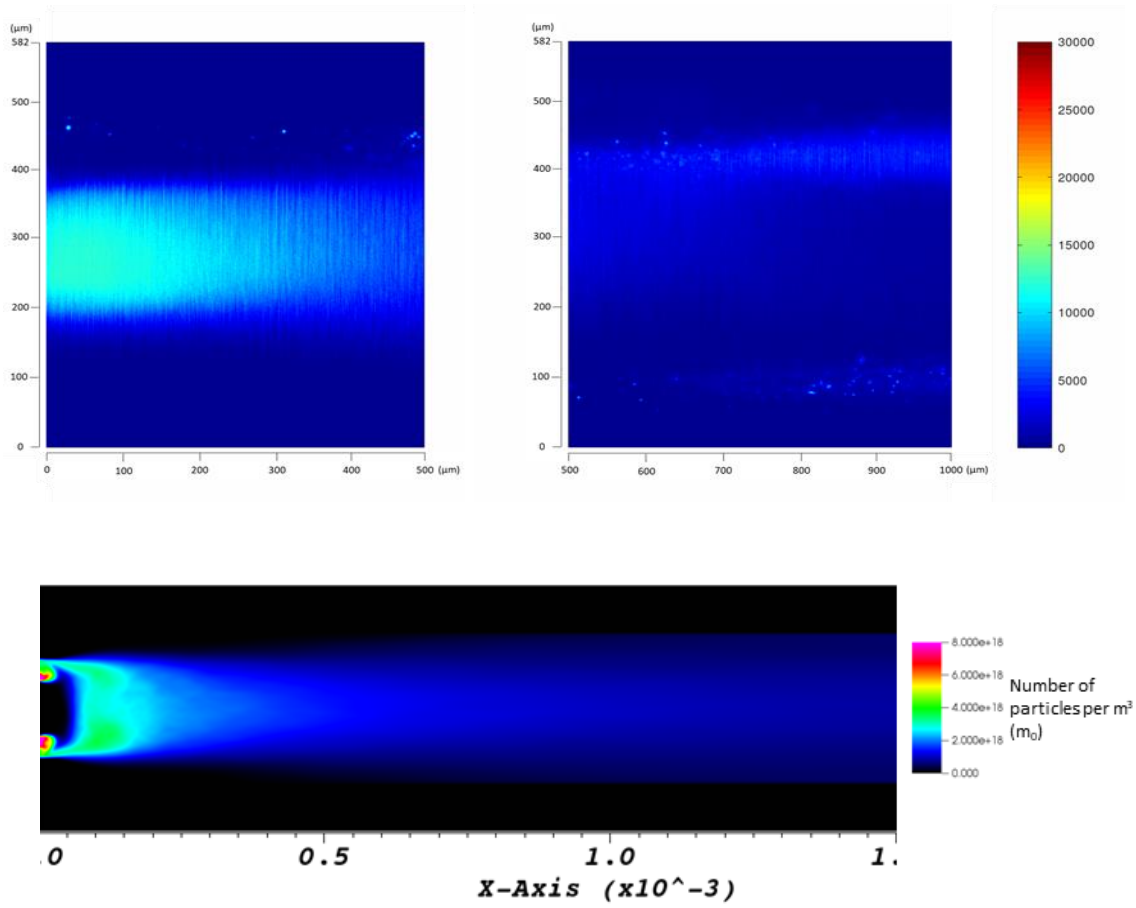

Figure 9: Mapping of cumulated intensity field of particles of BZX in the microchannel (top).
Simulation of particle number field in the microchannel having the same dimensions than the experimental one (down).

Discussion

In order to better understand the burst precipitation in the microchannel, we have analyzed the characteristic fields of the phenomena in the microchannel obtained by numerical simulation (Figure 10). This Figure represents the instantaneous 2D fields in the mid-plane of the reactor of the solubilized BZX concentration, the volume concentration of solid BZX particles, the supersaturation and the micromixing time calculated by the engulfment model developed by Baldyga and Bourne (Baldyga and Bourne, 1989), $t_m = 17.24\sqrt{\frac{\upsilon}{\varepsilon}}$ (with ε the dissipation rate of the turbulent kinetic energy and υ the kinematic viscosity).

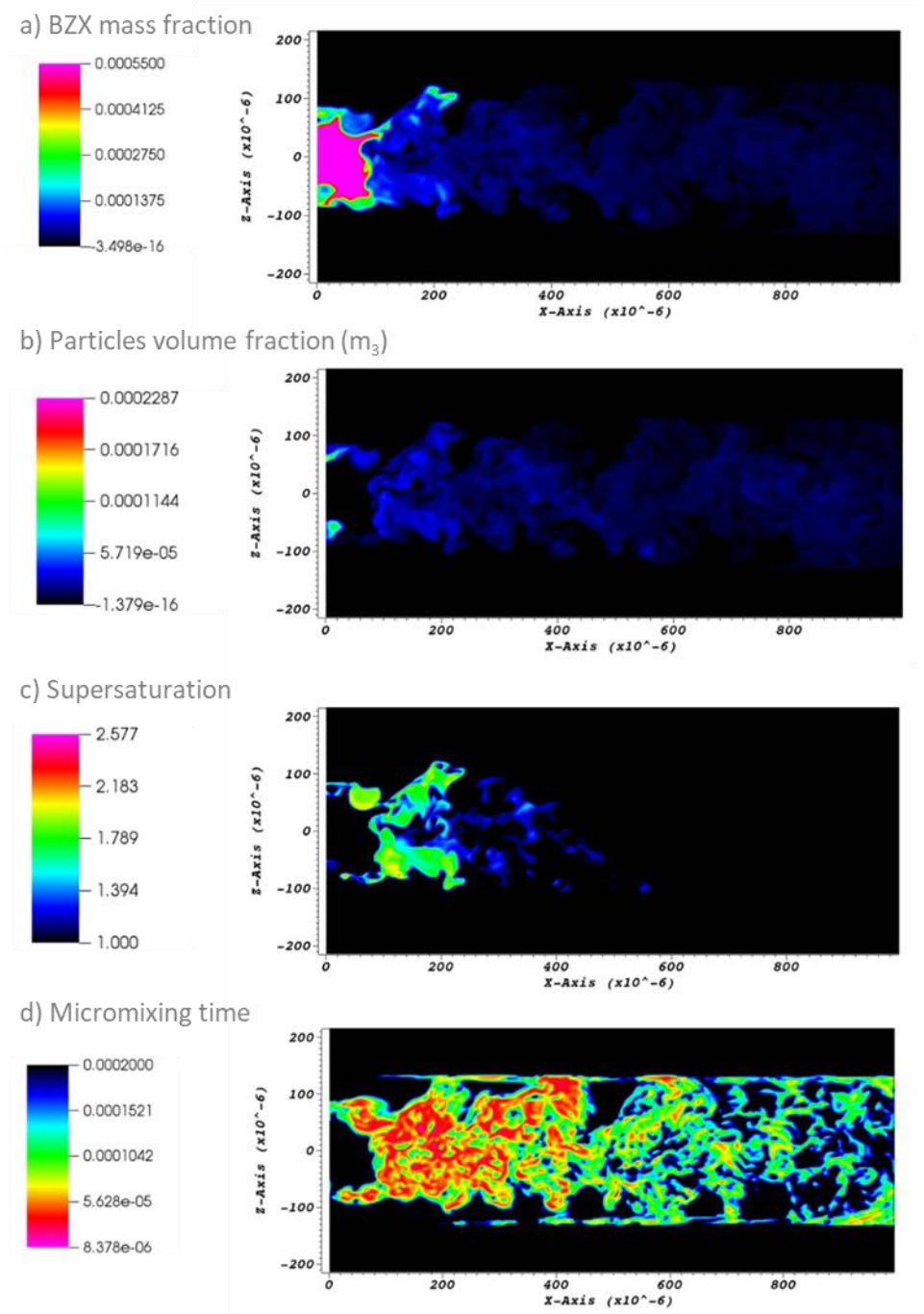

Figure 10: Instantaneous fields of the solubilized BZX mass fraction (a), third moment m_3 (volumetric concentration of solid BZX particles (m^3/m^3)) (b), the supersaturation (c) and the micromixing time (s) (d).

We observe a very strong mixing of BZX as soon as the compound leaves the injection on an extremely short length scale, thus with a very short time. The particles are then generated in this zone (Fig. 10b), which corresponds to a zone of important supersaturation (Fig. 10c). Figure 10d represents the mapping of local micromixing time and reveals very short micromixing times, lower than 10^{-4} s, and shows us that the intense mixing is located at the periphery of the central jet. These remarkable zones are well reflected in both numerical and experimental mappings. The mixing conditions are here very good, fast

and total, and show the importance of hydrodynamics in this type of reactor. These previous analyses of the numerical/experimental intensity fields have shown that the hypotheses put forward on the nucleation and growth mechanisms are quite consistent. However, when the size and particle distributions were compared in previous section (Fig. 7), a significant difference in terms of standard deviation or width of the distribution became apparent. The numerical distribution showed a distribution width almost twice as wide as the experimental one. In order to understand why such a wide numerical distribution, we have analyzed the different characteristic times of the precipitation, namely the mixing time (previously defined according to the Engulfment model), the growth time ($t_G = \left(\frac{M_p}{G\rho_p k_a m_2}\right) C_{sat}(S-1)$) (Makowski et al., 2012) and the nucleation time ($t_N = \frac{1}{VB}$, with B the nucleation frequency and V the volume of the mesh cell). For this purpose, we determined the volume distributions per time scale in the area close to the injector, where most of the precipitation takes place (Figure 12). The area indicated by the dotted box (Fig. 11) delimits the area for which the statistical analysis of characteristic times has been extracted.

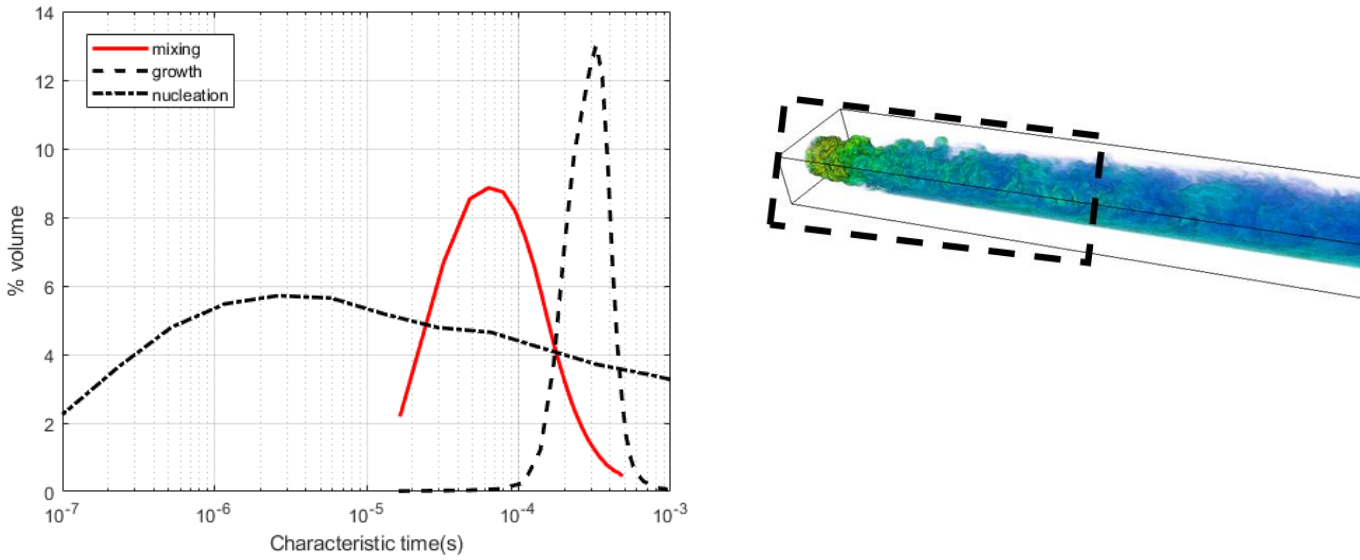

Figure 11: Distribution of mixing time, growth time and nucleation time.

The mixing time, well below 10^{-4} s, is very fast and conducive to rapid precipitation leading to small particles and a narrow particle size distribution. The growth time is greater than the mixing time by an order of magnitude. This is quite favorable to a homogeneous growth due to a very good prior mixing of the species. Again, this should naturally lead to a narrow particle distribution. The observation of the distribution of the nucleation times shows an average time around one order of magnitude below the mixing time (between 10^{-5} and 10^{-6} s). On the other hand, this distribution is spread over more than three orders of magnitude. This phenomenon is *a priori* responsible for obtaining a wide particle size distribution. In order to understand such a dispersion of nucleation times, corresponding to the inverse of the nucleation frequency, we determined the volume distribution of supersaturation levels (Fig. 12).

The supersaturation ranges from 1 to slightly over 2.2. We note a high proportion for relatively low levels of supersaturation, below 1.5. Finally, this relative dispersity of supersaturation levels (between 1 and 2) in the microchannel leads to nucleation kinetics that can differ up to several orders of magnitude. This can explain the width of the numerical size distribution of particles of BZX.

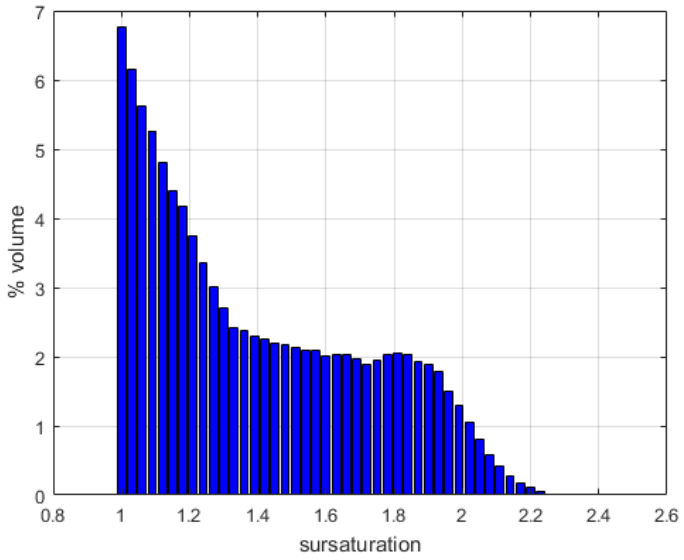

Figure 12: Distribution of supersaturation levels.

CONCLUSION

The µSAS process has shown its ability to produce small particles with a mean size of 16 (± 4) nm. These first results allowed us to adjust the fluid/solid interfacial tension with numerical simulation and estimate it at 4.75 mN/m. Moreover, thanks to the optical properties of the chosen fluorescent molecule, we have adopted an *in situ* analysis of the precipitation to have a better understanding of the nucleation and growth phenomena. This experimental result was successfully compared to the prediction given by numerical calculations and showed that the mixing is very fast (less than 10^{-4} s) and takes place totally in a very limited area at the outlet of the injector, leading to a domination of the homogeneous nucleation and thus to the formation of small particles. However, the particle size distribution calculated by simulation appeared wider than that obtained experimentally. The study of the supersaturation field in the microchannel showed some fluctuation of the supersaturation, which could be at the origin of a variation of the nucleation times.

Acknowledgement

We acknowledge the French National Research Agency for its support (ANR-17-CE07-0029 - SUPERFON), and the MCIA (Mésocentre de Calcul Intensif Aquitaine) and GENCI (DARI project number A0062A10815) for their HPC resources. We are also grateful to Dr. Nadine Leygue (SPCMIB, Université de Toulouse III) for the synthesis of the dye molecule.

References

Baldyga, J., Bourne, J.R., 1989. Simplification of micromixing calculations. I. Derivation and application of new model. The Chemical Engineering Journal 42, 83–92. https://doi.org/10.1016/0300-9467(89)85002-6

Bałdyga, J., Kubicki, D., Shekunov, B.Y., Smith, K.B., 2010. Mixing effects on particle formation in supercritical fluids. Chemical Engineering Research and Design, Special Issue – 17th International Symposium on Industrial Crystallization 88, 1131–1141. https://doi.org/10.1016/j.cherd.2010.02.016

Bremond, E., Leygue, N., Jaouhari, T., Saffon-Merceron, N., Erriguible, A., Fery-Forgues, S., 2021. Effect of substitution on the solid-state fluorescence properties of styrylbenzoxazole derivatives with terminal dicyanomethylene group. Journal of Photochemistry and Photobiology A: Chemistry 404, 112857. https://doi.org/10.1016/j.jphotochem.2020.112857

Ding, S., Anton, N., Vandamme, T.F., Serra, C.A., 2016. Microfluidic nanoprecipitation systems for preparing pure drug or polymeric drug loaded nanoparticles: an overview. Expert Opinion on Drug Delivery 13, 1447–1460. https://doi.org/10.1080/17425247.2016.1193151

Goda, K., 1979. A multistep technique with implicit difference schemes for calculating two- or three-dimensional cavity flows. Journal of Computational Physics 30, 76–95. https://doi.org/10.1016/0021-9991(79)90088-3

Guo, M., Song, H., Li, K., Ma, M., Liu, Y., Fu, Q., He, Z., 2020. A new approach to developing diagnostics and therapeutics: Aggregation-induced emission-based fluorescence turn-on. Medicinal Research Reviews 40, 27–53. https://doi.org/10.1002/med.21595

Ito, F., Oka, N., 2019. Use of Aggregation-Induced Emission for Selective Detection of Phase Transformation during Evaporative Crystallization of Hexaphenylsilole. Chemistry – An Asian Journal 14, 755–759. https://doi.org/10.1002/asia.201801563

Jaouhari, T., Zhang, F., Tassaing, T., Fery-Forgues, S., Aymonier, C., Marre, S., Erriguible, A., 2020. Process intensification for the synthesis of ultra-small organic nanoparticles with supercritical CO2 in a microfluidic system. Chemical Engineering Journal 397, 125333. https://doi.org/10.1016/j.cej.2020.125333

Jost, A.M.D., Glockner, S., Erriguible, A., 2020. Direct numerical simulations of fluids mixing above mixture critical point. The Journal of Supercritical Fluids 165, 104939. https://doi.org/10.1016/j.supflu.2020.104939

Makowski, łukasz, Orciuch, W., BaŁdyga, J., 2012. Large eddy simulations of mixing effects on the course of precipitation process. Chemical Engineering Science, 18th International Symposium on Industrial Crystallization 77, 85–94. https://doi.org/10.1016/j.ces.2011.12.020

Marre, S., Adamo, A., Basak, S., Aymonier, C., Jensen, K.F., 2010. Design and Packaging of Microreactors for High Pressure and High Temperature Applications. Ind. Eng. Chem. Res. 49, 11310–11320. https://doi.org/10.1021/ie101346u

Mei, J., Leung, N.L.C., Kwok, R.T.K., Lam, J.W.Y., Tang, B.Z., 2015. Aggregation-Induced Emission: Together We Shine, United We Soar! Chem. Rev. 115, 11718–11940. https://doi.org/10.1021/acs.chemrev.5b00263

Mersmann, A., 1999. Crystallization and precipitation. Chemical Engineering and Processing 9.

Roe, P.L., 1986. Characteristic-Based Schemes for the Euler Equations. Annual Review of Fluid Mechanics 18, 337–365. https://doi.org/10.1146/annurev.fl.18.010186.002005
Tran, V.L., Génot, V., Audibert, J.-F., Prokazov, Y., Turbin, E., Zuschratter, W., Kim, H.-J., Jung, J., Park, S.Y., Pansu, R.B., 2016. Nucleation and growth during a fluorogenic precipitation in a micro-flow mapped by fluorescence lifetime microscopy. New J. Chem. 40, 4601–4605. https://doi.org/10.1039/C5NJ03400K
Voisin, T., Erriguible, A., Philippot, G., Ballenghien, D., Mateos, D., Cansell, F., Iversen, B.B., Aymonier, C., 2017. Investigation of the precipitation of Na2SO4 in supercritical water. Chemical Engineering Science 174, 268–276. https://doi.org/10.1016/j.ces.2017.09.009
Wang, Y., Zhang, Y., Wang, J., Liang, X.-J., 2019. Aggregation-induced emission (AIE) fluorophores as imaging tools to trace the biological fate of nano-based drug delivery systems. Advanced Drug Delivery Reviews, Unraveling the In Vivo Fate and Cellular Pharmacokinetics of Drug Nanocarriers 143, 161–176. https://doi.org/10.1016/j.addr.2018.12.004
Wen, Y., Zhang, W., Gong, N., Wang, Y.-F., Guo, H.-B., Guo, W., Wang, P.C., Liang, X.-J., 2017. Carrier-free, self-assembled pure drug nanorods composed of 10-hydroxycamptothecin and chlorin e6 for combinatorial chemo-photodynamic antitumor therapy in vivo. Nanoscale 9, 14347–14356. https://doi.org/10.1039/C7NR03129G
Wilke, C.R., Chang, P., 1955. Correlation of diffusion coefficients in dilute solutions. AIChE Journal 1, 264–270. https://doi.org/10.1002/aic.690010222
Yadav, U.N., Kumbhar, H.S., Deshpande, S.S., Sahoo, S.K., Shankarling, G.S., 2015. Photophysical and thermal properties of novel solid state fluorescent benzoxazole based styryl dyes from a DFT study. RSC Adv. 5, 42971–42977. https://doi.org/10.1039/C4RA12908C
Yang, M.-Y., Zhao, R.-R., Fang, Y.-F., Jiang, J.-L., Yuan, X.-T., Shao, J.-W., 2019. Carrier-free nanodrug: A novel strategy of cancer diagnosis and synergistic therapy. International Journal of Pharmaceutics 570, 118663. https://doi.org/10.1016/j.ijpharm.2019.118663
Zhang, F., Erriguible, A., Marre, S., 2019. Investigating laminar mixing in high pressure microfluidic systems. Chemical Engineering Science 205, 25–35. https://doi.org/10.1016/j.ces.2019.03.063
Zhang, F., Marre, S., Erriguible, A., 2020. Mixing intensification under turbulent conditions in a high pressure microreactor. Chemical Engineering Journal 382, 122859. https://doi.org/10.1016/j.cej.2019.122859
Zhang, R., Xing, R., Jiao, T., Ma, K., Chen, C., Ma, G., Yan, X., 2016. Carrier-Free, Chemophotodynamic Dual Nanodrugs via Self-Assembly for Synergistic Antitumor Therapy. ACS Appl. Mater. Interfaces 8, 13262–13269. https://doi.org/10.1021/acsami.6b02416
Zhang, X., Li, N., Zhang, S., Sun, B., Chen, Q., He, Z., Luo, C., Sun, J., 2020. Emerging carrier-free nanosystems based on molecular self-assembly of pure drugs for cancer therapy. Medicinal Research Reviews 40, 1754–1775. https://doi.org/10.1002/med.21669
Zhao, Z., Zhang, H., Lam, J.W.Y., Tang, B.Z., 2020. Aggregation-Induced Emission: New Vistas at the Aggregate Level. Angewandte Chemie International Edition 59, 9888–9907. https://doi.org/10.1002/anie.201916729